Computers in Biology and Medicine 40 (2010) 687–697

Contents lists available at ScienceDirect

Computers in Biology and Medicine

journal homepage: www.elsevier.com/locate/cbm

Boundary detection in carotid ultrasound images using dynamic programming and a directional Haar-like filter

Yu-Bu Lee [a], Yoo-Joo Choi [b], Myoung-Hee Kim [c,*]

[a] Intelligent Systems Research Center, Sungkyunkwan University, Suwon, Republic of Korea
[b] Department of New Media, Korean German Institute of Technology, Seoul, Republic of Korea
[c] Department of Computer Science and Engineering, Ewha Womans University, Seoul, Republic of Korea

ARTICLE INFO

Article history:
Received 16 September 2008
Accepted 23 March 2010

Keywords:
Intima–media thickness
Directional Haar-like filter
Dynamic programming
Image feature
Boundary detection

ABSTRACT

The intima–media thickness (IMT) of the carotid artery, obtained from B-mode ultrasound images, has recently been proposed as one of the most useful indices of atherosclerosis and can also be used to predict major cardiovascular events. Ultrasonic measurements of the IMT are conventionally obtained by time-consuming manual tracing of the interfaces between tissue layers. We propose a computerized method to detect the boundary of the intima–media complex using a directional Haar-like filter that can account for the slope of the boundary in an image. The directional Haar-like filter extracts a directional boundary feature as an image feature in the region of interest, which is used to compute a cost function. A cost function includes not only the directional Haar-like filtering value but also the geometric continuity that is computed for every pixel in the region of interest. The optimal boundary pixels are detected by using a dynamic programming approach that searches for the pixel that minimizes the cost function in each column of the image. We compared the performance of the proposed method with that of manual methods performed by two radiologists. The results showed that our approach produces very similar results to those based on manual tracing, and there was no statistically significant difference between the IMT measurements segmented manually and those analyzed using our method.

1. Introduction

Carotid intima–media thickness (IMT) has proven to be an early marker of atherosclerosis and a strong predictor of future cardiovascular events such as stroke and myocardial infarction [1]. An increased IMT is also associated with the prevalence of cardiovascular disease and is involved in atherosclerosis in other arterial systems [2–4]. The IMT of the carotid artery is usually measured using a high resolution B-mode ultrasound image, because it is noninvasive, safe, inexpensive, and relatively simple. Most researchers have traced the intima–media complex (IMC) manually to determine the IMT. However, the conventional manual tracing method has the drawback of inconsistency since the performance is dependent on the subjective judgment of an observer. Moreover, this procedure is very time consuming. Therefore, this method is inappropriate for projects requiring high consistency, such as analyzing a large database of carotid artery sonographic images.

To avoid these problems, various computerized methods have been proposed for detecting the IMC in carotid artery images. Selzer et al. [5] described a multi-step procedure. In their method, the approximate position of the boundary is identified first by manually placing a small number of points on the vessel interface. Guided by this approximation, a set of conditional edges is generated by applying a maximal local intensity gradient criterion. The strengths of these edges are then evaluated and weak edges are eliminated. Obviously, the subjectivity by an observer is not completely eliminated since an initial input is required.

Dynamic programming has been used to detect the boundaries of the intima–media [6–8] from multiple-image features such as intensity and gradient. These methods produce reproducible measurements of the ultrasonic data, but some subsequent manual correction is required. In addition, the process involves three weighting factors that have to be tuned using a training procedure [8], which is based on tracings by experts.

Cheng et al. [9] suggested using the snake approach [10] to detect the boundaries of the intima–media complex. This approach is very sensitive to the initial approximation of the contour, which must be placed close to the actual boundary of interest or the snake will not be attracted. In addition, the

* Corresponding author. Tel.: +82 2 3277 2315; fax: +82 2 3277 4409.
E-mail addresses: yubulee23@hotmail.com (Y.-B. Lee), mhkim@ewha.ac.kr (Y.-J. Choi), basilia@skku.edu (M.-H. Kim).

0010-4825/$ - see front matter © 2010 Elsevier Ltd. All rights reserved.
doi:10.1016/j.compbiomed.2010.03.010

weighting factors representing elasticity and rigidity have to be tuned. Cheng and Jiang [11] subsequently proposed another automated procedure that uses dual dynamic programming. This method is based on a cost function that includes geometric constraints constructed using anatomical knowledge. This approach is less affected by speckle noise than previous dynamic programming techniques [8]. However, additional weighting factors are required to smooth the dual curve, and these must be tuned to match the characteristics of the particular ultrasound instrumentation. More recently, Loizou et al. [12] revisited the snake approach. They preprocessed ultrasound data by normalization and speckle reduction, and then used an improved procedure for initializing the snake. However, the ability of this technique to deal with irregular boundaries was not investigated.

In this paper, we present a semi-automatic boundary detection procedure based on dynamic programming and use of a directional Haar-like filter. We use dynamic programming [13] to achieve a global minimum search of image features extracted using a directional Haar-like filter. Our method uses a Haar-like filter to take into account the slope of the boundary, whereas most previous works have not dealt with the sloping boundaries that occur in carotid artery images. By applying a directional Haar-like filter, we were able to increase the robustness of edge detection against speckle noise, weak edges and echo gaps in the ultrasound images.

The rest of this paper is organized as follows: in Section 2, we describe our image acquisition techniques and the characteristics of carotid artery ultrasound images. We also describe the segmentation procedure that we use to detect the boundary of the intima and adventitia layers. The results from this method are evaluated in Section 3. Finally, we draw some conclusions in Section 4.

2. Materials and methods

The B-mode longitudinal ultrasound images of the common carotid artery used in this study were acquired using an Accuvix XQ (Medison Co. Ltd., South Korea) ultrasound scanner with a linear 5–12 MHz transducer. The artery was examined by turning the neck of the subject to the left and right, with the transducer positioned at the side of the neck. This approach maximizes the lumen in the longitudinal plane so as to produce a good image of the near and far wall of the artery. The intima–media complex of the artery is identified by characteristic double lines. The images were then saved in DICOM format using the SonoView software.

2.1. Image characteristics

A representative image of the carotid artery is shown in Fig. 1(a). The near and far walls of this artery are made up of the adventitia, media and intima, which are distinct tissue layers. Fig. 1(b) shows a close-up of the region of interest in Fig. 1(a), consisting of the echo zones Z1–Z4 and the vessel interfaces I1 and I2, which correspond to the intima–media complex at the far wall of the carotid artery. The leading edges I1 and I2 of echo zones Z2 (intima) and Z4 (adventitia) are, respectively, the lumen–intima and media–adventitia interfaces of the far wall.

The IMT is defined as the distance between I1 and I2. As shown in Fig. 1(a), the echo zones of the near wall are weaker than those of the far wall, due to the overlap of echo pulses. Therefore, the lumen–intima and media–adventitia interfaces of the far wall is the preferred site for the IMT measurements. Manual measurements of the IMT are made by placing calipers on the leading edges I1 and I2, which are traced manually. A close-up image of the intima-–media complex at the far wall of the artery and the calipers are shown in Fig. 2(a). Fig. 2(b) illustrates the placement of calipers on the anatomical structures of the far wall of the artery.

2.2. An image feature based on a directional Haar-like filter

2.2.1. Problem statement

Detecting the boundaries of the intima and adventitia layers of the carotid artery from ultrasound images is challenging because of speckle noise, imaging artifacts and weak edges due to random scattering. In addition, some parts of an image may be missing because of echo dropout or acoustic holes, which increase the difficulty of detecting the correct boundaries. Additionally, the IMC is not completely horizontal in the image, due to variables such as the position and the angle of the probe with respect to the arterial wall during the acquisition of the images. To overcome the difficulty, we combine a global optimization approach using dynamic programming with the use of a directional Haar-like filter.

2.2.2. Cost function

Cost functions are built for I1 and I2. If a user specifies an $M \times N$ region of interest, all possible boundaries B_N can be considered as polylines with N nodes:

$$B_N = \{\boldsymbol{p}_1, \boldsymbol{p}_2, \ldots, \boldsymbol{p}_{N-1}, \boldsymbol{p}_N\}, \tag{1}$$

where the pixels $\boldsymbol{p}_{N-1}$ and $\boldsymbol{p}_N$ are horizontal neighbors, and N is the horizontal length of a contour line. The cost function $C(B_N)$ is defined as the following sum of local costs along a candidate boundary B_N:

$$C(B_N) = c_f(\boldsymbol{p}_1) + \sum_{i=2}^{N} (w_1 c_f(\boldsymbol{p}_i) + w_2 c_g(\boldsymbol{p}_{i-1}, \boldsymbol{p}_i)). \tag{2}$$

At a point $\boldsymbol{p}_i$, the local cost is made up of two terms, an image feature term $c_f(\boldsymbol{p}_i)$ and a geometrical force term $c_g(\boldsymbol{p}_{i-1}, \boldsymbol{p}_i)$.

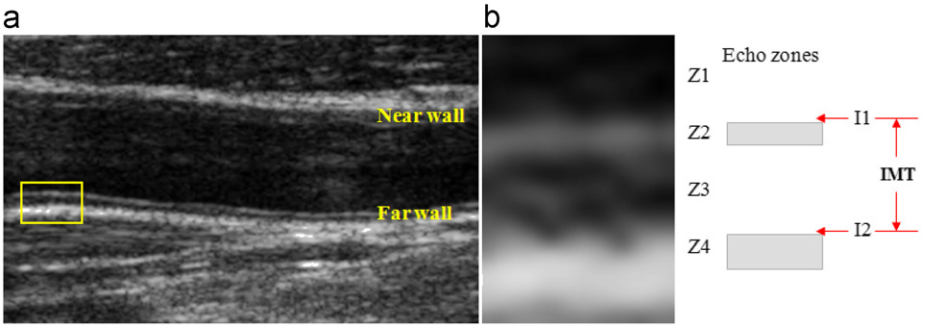

Fig. 1. The intima–media complex of the carotid artery: (a) B-mode ultrasound image of the arteryand (b) echo zones and interfaces corresponding to the intima–media complex of the far wall of the artery.

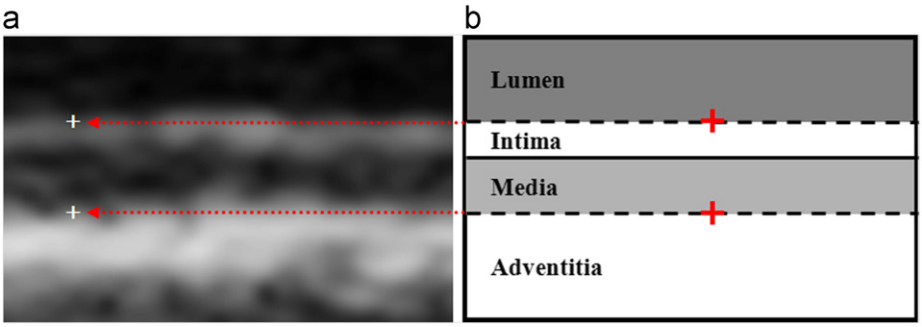

Fig. 2. Using calipers for manual measurement of the IMT: (a) close-up image with calipers and (b) placement of calipers on the anatomical structures of the far wall of the carotid artery.

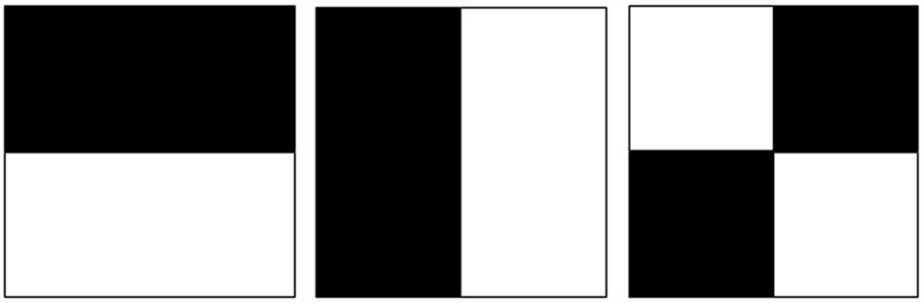

Fig. 3. The different types of Haar filters.

In Eq. (2), w_1 and w_2 denote weighting factors of the image feature term and the geometrical force term, respectively, under the constraint $w_1+w_2=1$. w_1 enhances the image property based on intensity, while w_2 controls the smoothness of the boundary. The relative importance of each term can be controlled by tuning these two factors. To design a robust automatic system for extracting the intima and the adventitia layers, we empirically determined these two factors based on 75 test images that included various types of noise conditions. We used $w_1=0.9$ and $w_2=0.1$ for all test images as constants. We show the empirical analysis results for determining the weighting factors in Section 4.

2.3.1. Cost terms

The terms in the cost function associated with each of the boundaries I1 and I2 must reflect the geometry of that boundary and the characteristics of the image features in its vertical neighborhood. These cost terms are defined in such a way that a stronger image feature at $\boldsymbol{p}_i$ will yield a lower local cost. The resulting boundary is the polyline B_N that minimizes the cost function $C(B_N)$.

In the previous investigation, the authors [8] used an image feature term that combined three costs: the average intensity of k pixels below a pixel $\boldsymbol{p}_i$, the average intensity of l pixels above a pixel $\boldsymbol{p}_i$, and the downward intensity gradient, which is estimated as the vertical slope at the center of a third-order polynomial surface fitted to the intensity values within a 5×5 window. The geometrical force term $c_g(\boldsymbol{p}_{i-1}, \boldsymbol{p}_i)$, which is designed to ensure the continuity of borders, is defined as follows:

$$c_g(\boldsymbol{p}_{i-1},\boldsymbol{p}_i)=|d(\boldsymbol{p}_i)-d(\boldsymbol{p}_{i-1})|^2 \quad (i=2,\ldots,N), \tag{3}$$

where d is the vertical distance between the boundary being estimated and a reference line at a node. That is, $c_g(\boldsymbol{p}_{i-1}, \boldsymbol{p}_i)$ denotes the range that node $\boldsymbol{p}_{i-1}$ in the previous column is allowed to jump onto node $\boldsymbol{p}_i$ in the current column. The geometrical force term for I2 is calculated with respect to a horizontal reference line. In estimating the cost term for I1, the reference line is the border I2 that has already been detected.

For computing the cost function, we adopt a new image feature term using a modified Haar filter with the geometrical force term of the previous method [8]. Haar filters originate from Haar basis functions. Viola and Jones [14] proposed an efficient algorithm for face detection using the Haar filters, which can be represented as a number of connected black and white rectangles. The output of this filter is the difference between the sums of the pixel values within two rectangular regions:

$$f_h=\sum_{i,j\in R_{black}} I(x_i,y_j)-\sum_{k,l\in R_{white}} I(x_k,y_l), \tag{4}$$

where R_{black} and R_{white} are the black and white areas of the template, and $I(x, y)$ is the intensity value at pixel (x, y). Three elementary types of Haar filters capture changes in intensity along the horizontal, vertical, and the diagonal directions as shown in Fig. 3.

We adopted the horizontal Haar filter to calculate the image feature term. Knowing that the boundaries I1 and I2 are located below a bright region and above a dark region of the IMC layer, as shown in Fig. 4, we modified the Haar filter by adding a third region between the other two, to correspond to a pixel-wide boundary located between the dark and bright regions.

Fig. 5(a) shows a basic Haar-like filter of this type that can only detect a horizontal boundary. To estimate the image feature term for a sloping boundary, we create a directional Haar-like filter by rotating the basic Haar-like filter so that it is aligned with the slope of the boundary. If $\boldsymbol{p}_i$ is a pixel at (x, y), then the image feature term $c_f(\boldsymbol{p}_i)$ in Eq. (2) is defined as follows:

$$c_f(x,y)=\min_{\alpha\in\{-45^\circ,-40^\circ,\ldots,40^\circ,45^\circ\}}(f_{h_\alpha}(x,y))(x,y\in R^2),$$

$$f_{h_\alpha}(x,y)=\sum_{j=1}^{w}\Bigg(\sum_{k=-(h-1)/2}^{-1} I(\mathrm{rot}_\alpha(x+j,y+k)) - \sum_{k=1}^{(h-1)/2} I(\mathrm{rot}_\alpha(x+j,y+k))\Bigg) \quad (h\geq 3, h \text{ is odd}), \tag{5}$$

where R^2 denotes the spatial coordinates of an image and α is the rotation angle of the Haar-like filter. The function $rot_\alpha(x+j, y+k)$ returns the x and y coordinate values of a pixel $(x+j, y+k)$ $[1 \le j \le w, -(h-1)/2 \le k \le -1$ and $1 \le k \le (h-1)/2]$ in the black and white regions when the filter is rotated by α degrees around its central pixel (x, y). I denotes the intensity values at pixel (x, y), and w and h denote the width and height of the filter, respectively. The value of $c_f(x, y)$ is normalized to the range of $[0, 1]$ to eliminate the effect of image size. Fig. 5(b) shows how we rotate the filter around each pixel through angles in the range $[-45°, 45°]$ in five-degree intervals. The maximum and minimum values of rotation correspond to clinical practice, in which it is assumed that the slope of the intima and adventitia layers in carotid artery images used for measuring IMT will not exceed $-45°$ or $45°$.

The image feature term is the minimal value of the difference between the sums of the pixel values within the two rectangular regions of the Haar-like filter at each angle of rotation. This value is then stored at the central pixel of the filter. The angle of rotation that is closest to the slope of the boundary will yield the minimum of the image feature term. Fig. 6 illustrates the comparison between a normal Haar-like filter that is not rotated and a rotated Haar-like filter on an oblique edge. Using the rotated Haar-like filter, we can see that the black and white regions correctly correspond to dark and bright layers, respectively, whereas the normal Haar-like filter fails to match each region to its corresponding layer accurately. The cost terms for I1 are similar to those for I2, except for the size of the filter.

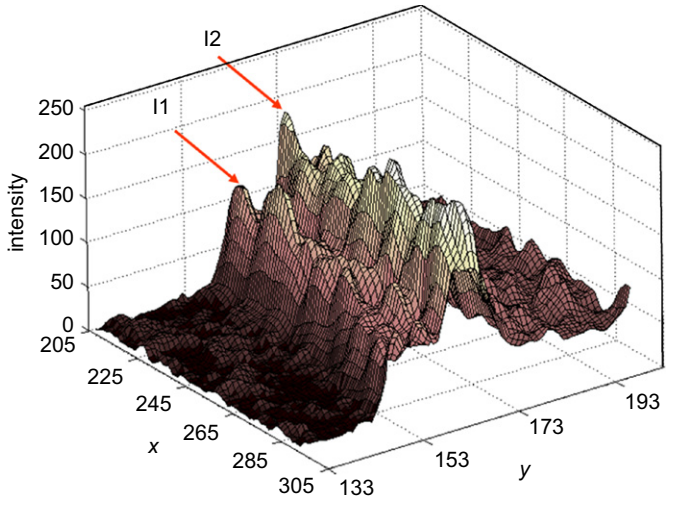

Fig. 4. Image of the intima–media complex, with intensity plotted as height.

3. Boundary detection using dynamic programming

Dynamic programming is a popular method for optimization problems, and can be used for border detection through minimization of the cost function $C(B_N)$. The search for a solution must be performed globally in the region of interest so as to avoid local minima due to interference patterns such as speckles. To recast our problem as a global optimization approach using dynamic programming, we begin by rewriting Eq. (2) in a recursive form, as follows:

$$\begin{aligned} &C(B_1) = c_f(p_1), \\ &C(B_n) = C(B_{n-1}) + (c_f(p_n) + c_g(p_{n-1}, p_n)) \quad (n = 2, \ldots, N). \end{aligned} \tag{6}$$

If the candidate minima of the cost function of the polyline B_N are written as $\tilde{C}(B_n)$, we can rewrite these equations as a multistage cost accumulation process:

$$\begin{aligned} &\tilde{C}(B_1) = c_f(p_1), \\ &\tilde{C}(B_n) = \min_{p_{n-1}} \{\tilde{C}(B_{n-1}) + (c_f(p_n) + c_g(p_{n-1}, p_n))\} \quad (n = 2, \ldots, N). \end{aligned} \tag{7}$$

We can then use this equation to search for the optimal border by accumulating costs, while storing the location of $\boldsymbol{p}_{n-1}$, which defines $\tilde{C}(B_n)$, in a pointer array at each stage n. Fig. 7 shows the cost surface for the ROI. As shown in Fig. 7(b), cost values corresponding to the boundary cause the polyline to go along a path approximating the valley, which is the global minimum of the cost function for an optimal border.

We will now describe the cost accumulation and backtracking process in detail for an $M \times N$ region. A vertical window of height M is used to scan the boundary from left to right across N horizontal positions. The locations of the start and end-point are the upper-left and upper-right pixels of the region, respectively, corresponding to the left and right arrows in Fig. 8(b). For each column n, a candidate minimum of the cost function is found for each pixel, and its cost is accumulated. After scanning all the columns, we search a point with minimum accumulated cost at the last column. This position becomes the end-point of the boundary as well as the starting-point for backtracking. Then backtracking is performed by following the arrows shown in Fig. 8(a), until the first column in the ROI is reached. Each arrow points to the pixel in the previous column with the minimum accumulated cost, so that

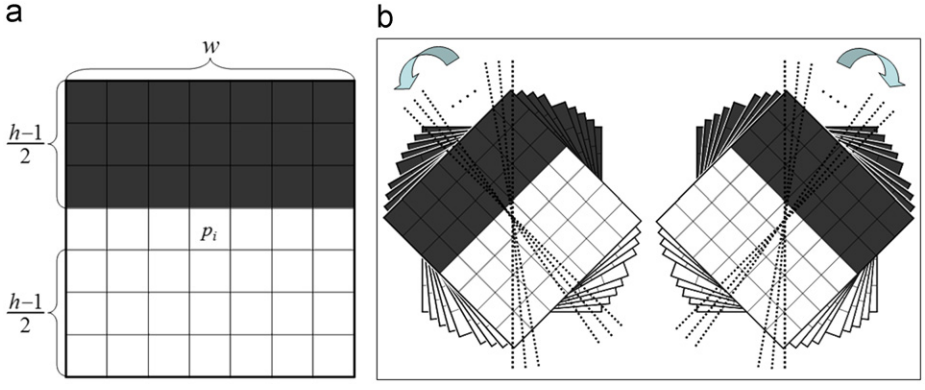

Fig. 5. The directional Haar-like filter: (a) a basic Haar-like filter of size $w \times h$ and (b) Haar-like filters rotated through $[-45°, 45°]$ at $5°$ intervals.

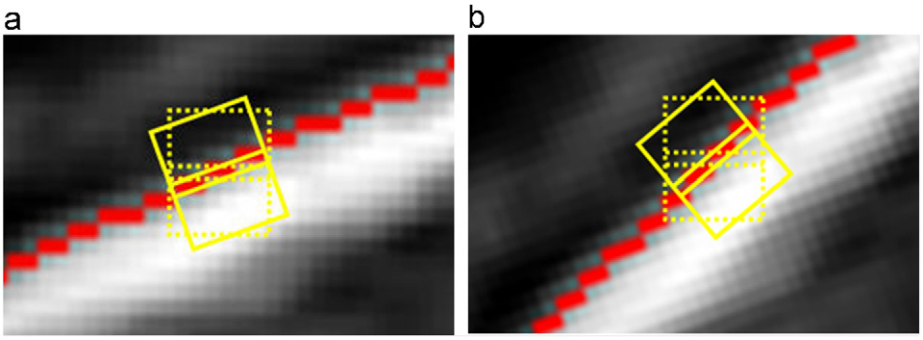

Fig. 6. Examples of comparisons between a basic Haar-like filter (rectangle with dotted line) and the directional Haar-like filter (rectangle with solid line) on an edge with slopes of (a) -20° and (b) -40°.

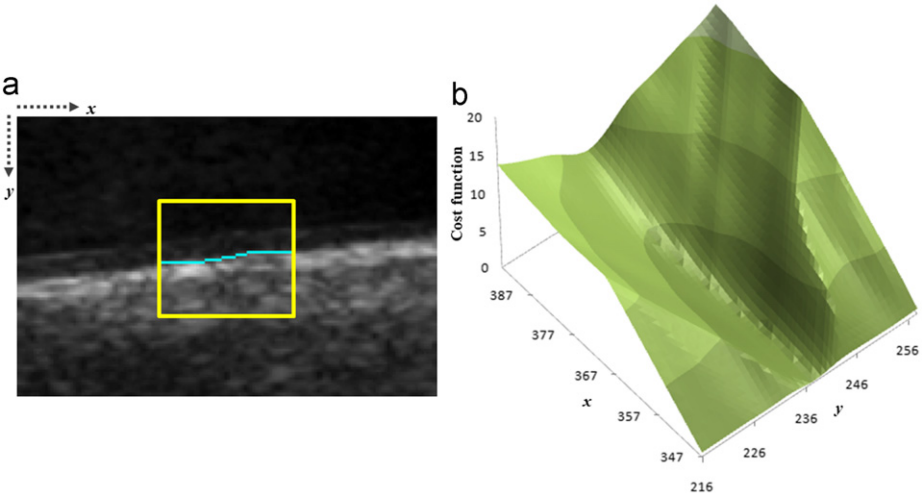

Fig. 7. Cost surface for the ROI: (a) the media–adventitia boundary detected in the ROI of the carotid artery image and (b) cost surface based on cost values of every pixel in the ROI.

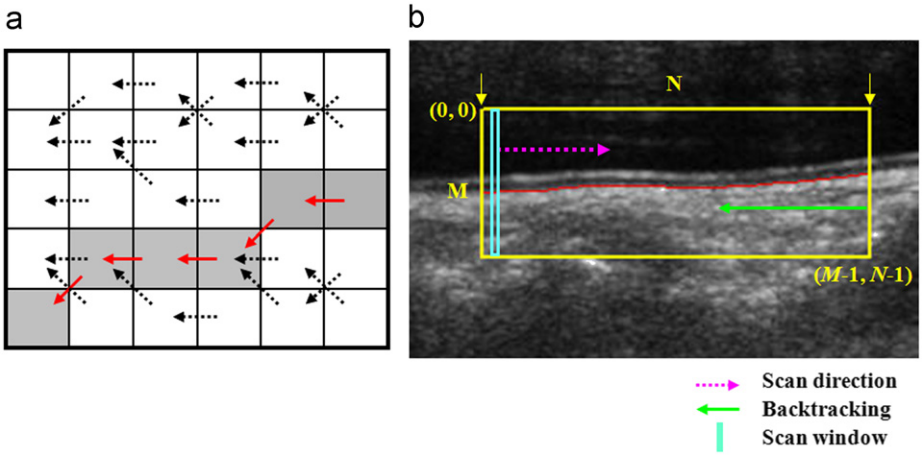

Fig. 8. Boundary detection using dynamic programming: (a) the backtracking process and (b) detecting the media–adventitia boundary in the carotid artery image.

backtracking finds the pixels on the border. This creates our estimate of the boundary. We find I2 first, because it can be identified relatively easily since the nearer echogenic zone Z4 is stronger than Z2. We then search for I1 using a smoothened version of I2 as the reference line, which forms a lower limit to the search.

4. Experimental results

Our method has been applied to 20 B-mode carotid artery ultrasound images covering a wide range of scanning conditions and boundary slopes. The images had a resolution of 640×480 pixels with a pixel size of 0.09 mm. The segmentation results were

evaluated by visual inspection, accuracy evaluation, and processing time. For visual inspection, we compared our results and those from a previous dynamic programming technique [8].

Figs. 9 and 10 show the accurate detection of boundaries with slopes of less than 5° and greater than 5°, respectively. We compared our method with a previous dynamic programming

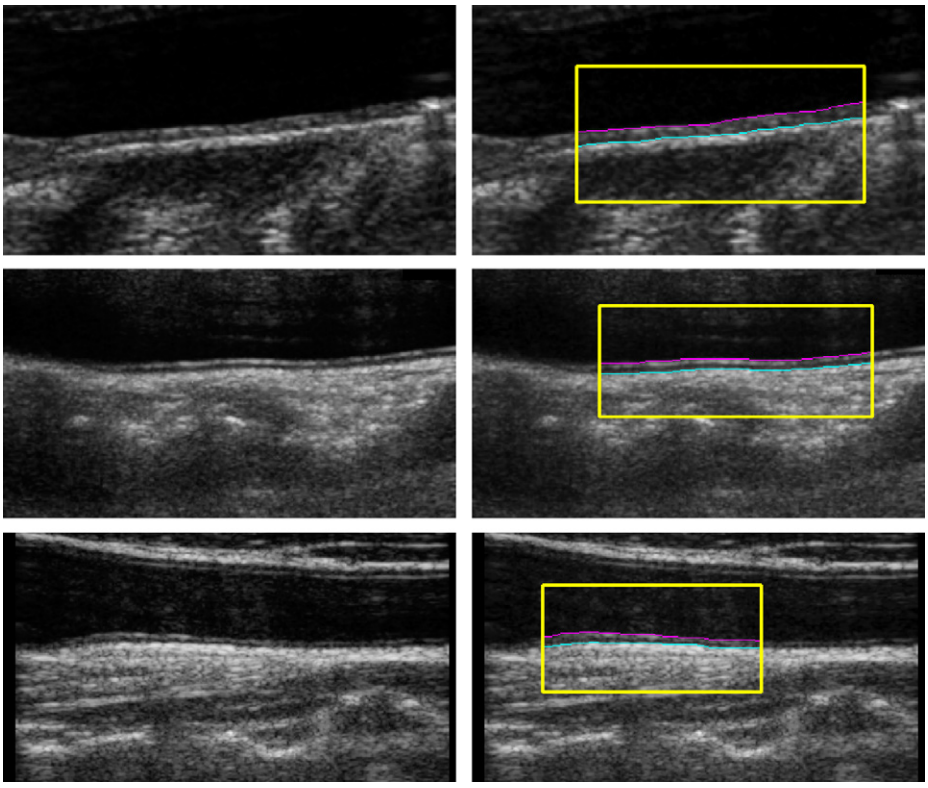

Fig. 9. Experimental results for horizontal boundaries. Left: original image and right: detected boundaries of the intima and adventitia layers.

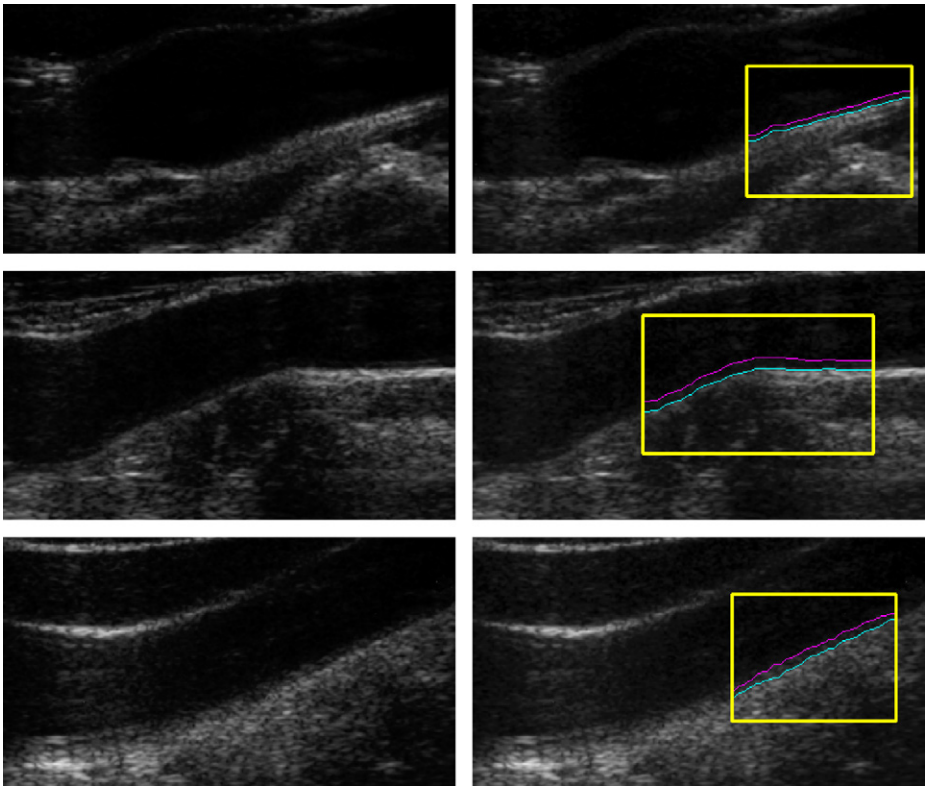

Fig. 10. Experimental results for sloping boundaries. Left: original image and right: detected boundaries of the intima and adventitia layers.

technique for sloping boundaries in Fig. 11. By comparing Fig. 11(a) and (c), we can see that our approach produces more accurate and smoother segmentations. We believe that this is because our technique explicitly accounts for the slope of the boundary. Fig. 12 illustrates that our method accurately detected boundaries against high levels of noise such as speckles.

We also compared our method with the previous dynamic programming technique for images with an echo gap, which causes difficulties in detecting the boundary correctly. Fig. 13(a) and (c) illustrate that the previous dynamic programming method did not overcome the problem of an echo gap on the adventitia, while our method performs well even in the presence of an echo gap and a sloping boundary. Fig. 14 shows the result of boundary detection from the obscure image with severe echo dropout on the intima by our method.

The error between the results of the proposed method and those of manual tracing was measured to investigate the accuracy of the proposed method. Manual tracing was performed by two

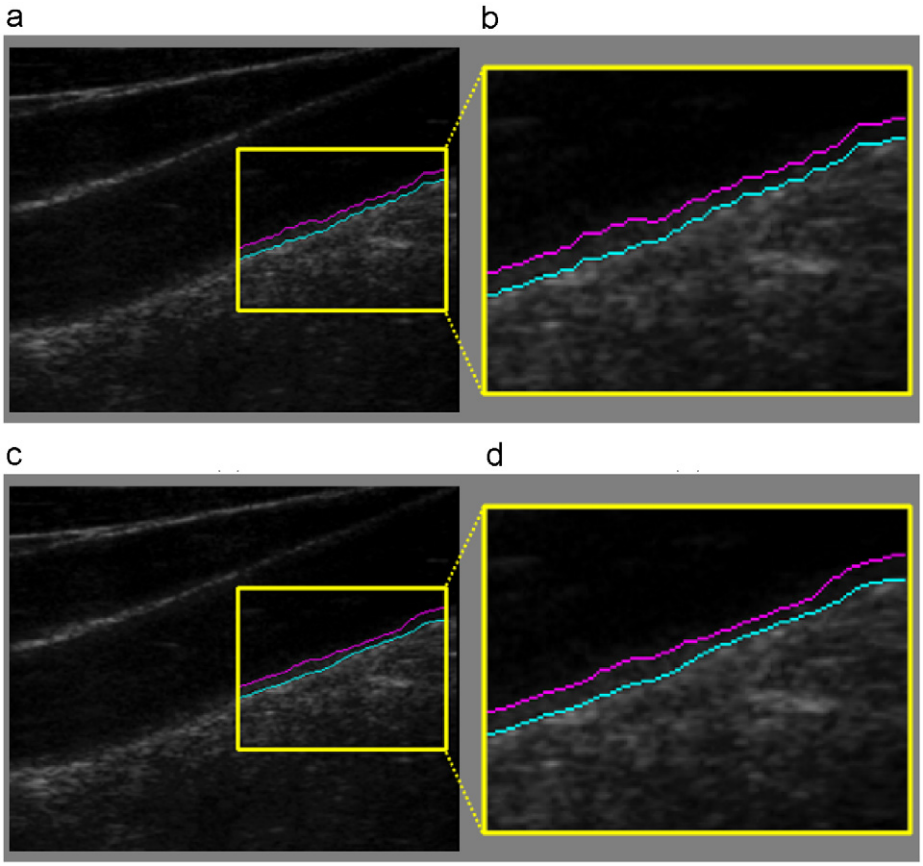

Fig. 11. Detecting sloping boundaries using: (a) and (b) (enlarged) the previous dynamic programming technique; (c) and (d) (enlarged) our method.

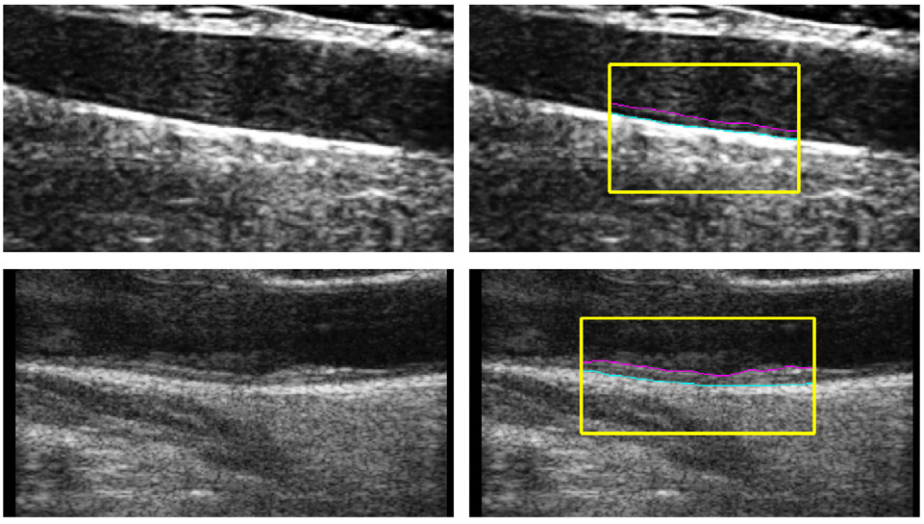

Fig. 12. Boundary detection result from an indistinct image with speckles. Left: original image and right: detected boundaries of the intima and adventitia layers.

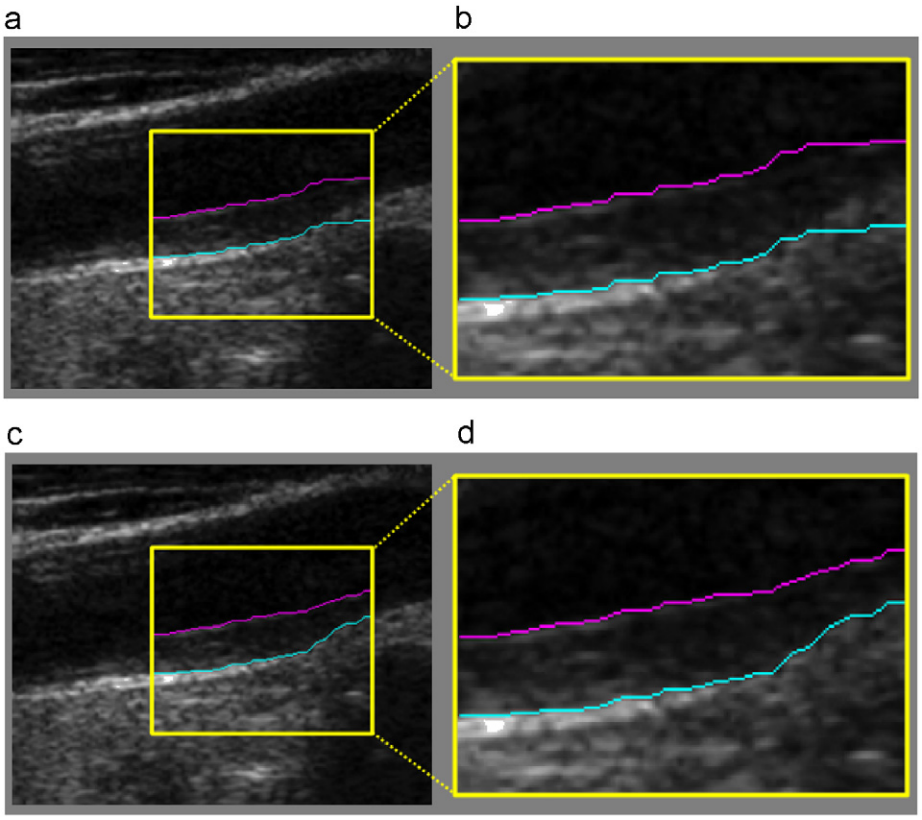

Fig. 13. Detecting boundaries in the presence of an echo gap on the adventitia using: (a) and (b) (enlarged) the previous dynamic programming technique; (c) and (d) (enlarged) our method.

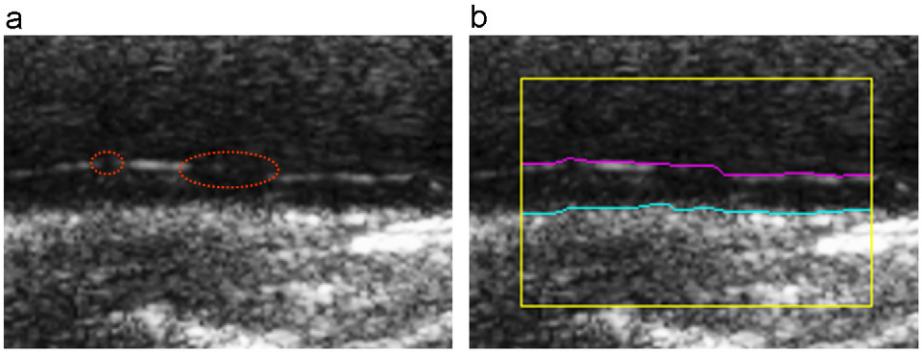

Fig. 14. Result of boundary detection from the obscure image with severe echo dropout on the intima: (a) original image; (b) boundaries detected by our method.

radiologists and the results of each manual tracing for an image were averaged to form a standard boundary. The boundary detection error [9] in an image was calculated as the mean of the absolute distance in the vertical direction between the corresponding pairs of pixels on the boundaries detected by our method and by manual tracing as follows:

$$\mathrm{Err} = \frac{1}{n}\sum_{i=1}^{n} |ay_i - my_i|, \tag{8}$$

where ay_i and my_i denote the y-coordinate value of the ith point in the x direction on the boundaries detected by our method and by manual tracing, respectively, and n is the length of the boundary in the x direction.

To validate the improvements of the proposed method, we compared the errors of our method with those of the previous dynamic programming technique. By analyzing the experiments using images with various types of noise, we validated that the proposed method is insensitive to the influence of speckles, echo gap and dropout. Fig. 15 shows the errors for the proposed method and the previous dynamic programming method with respect to manual tracing. The errors were calculated for each leading edge I1 (Fig. 15(a)) and I2 (Fig. 15(b)) of the intima and adventitia layers on twenty images. These images were varied and included features such as the presence of the sloping boundary (test image number 1–12), speckle noise (test image number 13–15), echo gap (test image number 16–18), and dropout (test image number 19 and 20). In the case of I1, the error ranged from 0.05 to 0.11 mm for the previous dynamic programming technique and from 0.03 to 0.05 mm for our method, respectively. In the case of I2, the difference between the previous dynamic programming technique and manual tracing

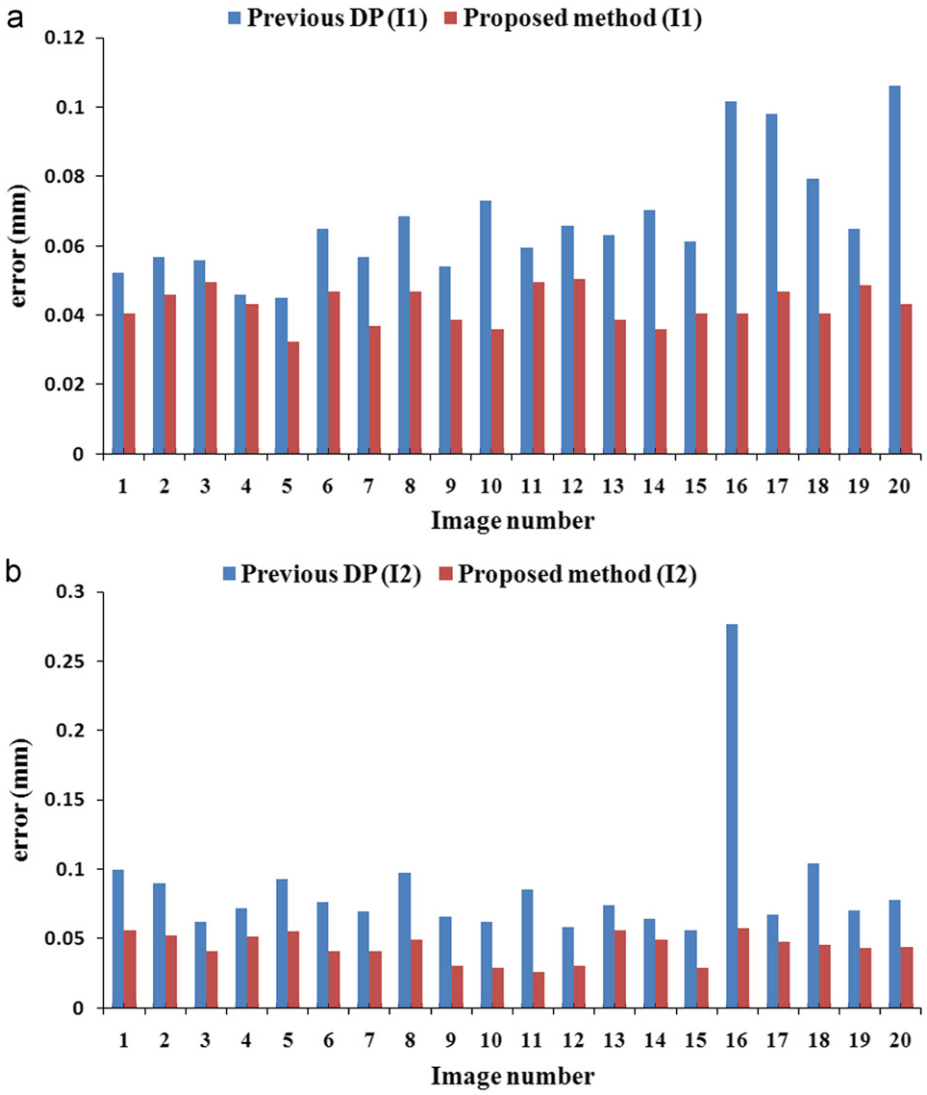

Fig. 15. The error of our method and the previous dynamic programming technique compared to manual tracing from the leading edge of: (a) the intima layer and (b) the adventitia layer.

ranged from 0.06 to 0.28 mm, while the error of our method ranged from 0.03 to 0.06 mm. As shown in Fig. 15, our method has smaller errors than the previous dynamic programming method in the detection of both boundaries (I1 and I2). In particular, it has been proven that our approach is insensitive to speckles, an echo gap, and dropout by the stable errors of images 13–15 that included speckle (for Fig. 12(a) and (b)), images 16–18 that included an echo gap (for Fig. 13), and images 19 and 20 with dropout (for Fig. 14).

For determining the weighting factors, we analyzed 75 images that included various image features. Test images are classified into 5 different groups by the boundary and image features, and include horizontal boundary (horizontal image), sloping boundary (sloping image), speckle noise (speckle image), echo gap noise (echo gap image), and dropout noise (dropout image). In this study, our method includes two cost function terms and hence two weighting factors, w_1 for the image feature term and w_2 for the geometric force term with the constraint $w_1+w_2=1$. We applied our boundary detection procedure using each combination of (w_1, w_2) changed by a step of 0.1 to the test images and then computed the error for each combination of (w_1, w_2). In the parameter space, the value of (w_1, w_2) associated with the lowest average error is empirically selected as the best combination of the weighting value. Fig. 16 shows the average error with respect to each combination (w_1, w_2) of weighting values. Fig. 16(a) illustrates the average error computed from 75 images and Fig. 16(b) shows the average error separately from each group of images according to each combination (w_1, w_2). As shown in Fig. 16, the average error was the lowest in all cases when the weighting value (w_1, w_2) is (0.9, 0.1). Therefore, we determined that 0.9 and 0.1 would be used for weighting factors w_1 and w_2, respectively.

To determine whether the paired measurements of two different methods differ from each other in a significant way, the paired t-test was applied to the 20 IMT_{max} and 20 IMT_{min} measurements collected above [15]. The p-value obtained by the paired t-test from the IMT_{max} was 0.572 for automatic measurements (Automatic) by our method versus manual measurements by expert 1 (Manual1) and 0.6 for automatic versus manual measurements by expert 2 (Manual2), respectively. The p-value from the IMT_{min} was 0.542 for Automatic versus Manual1 and 0.887 for Automatic versus Manual2, respectively. Since all p-values were larger than 0.05, there was no significant difference between the IMT measurements of the IMC segmented by our method versus the manual method.

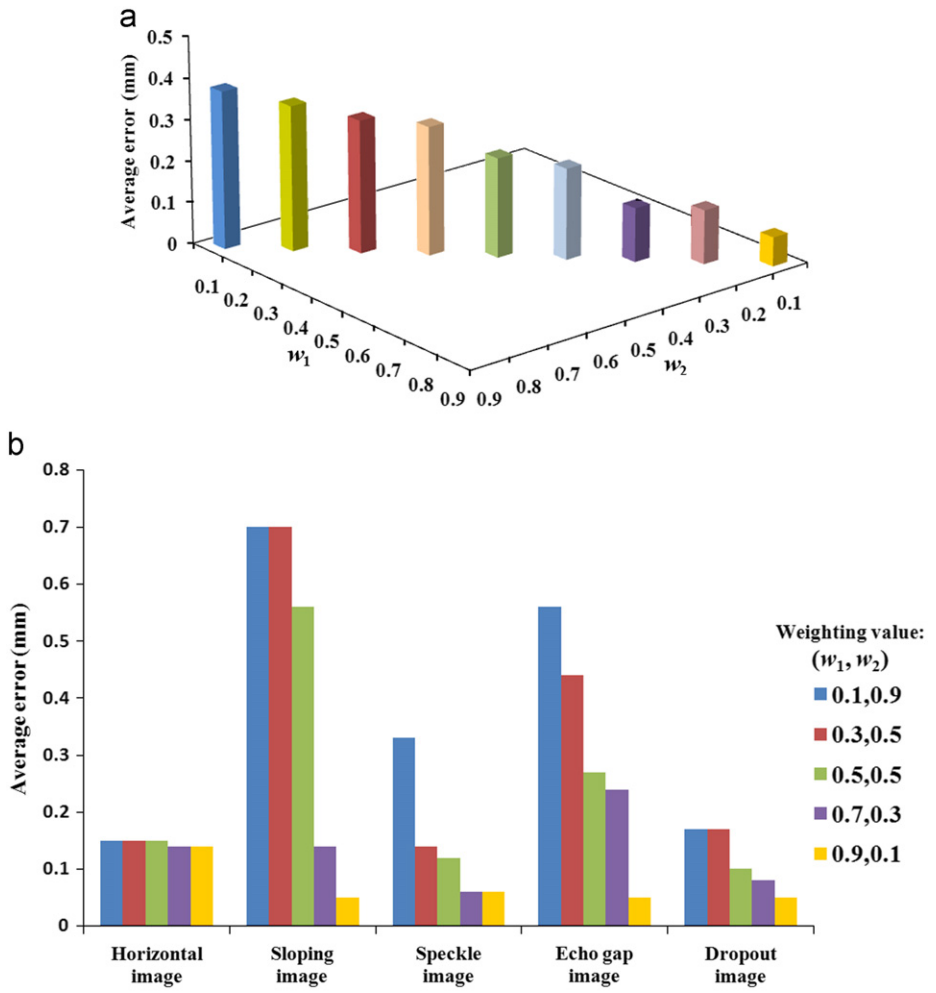

Fig. 16. The average of errors for the proposed method with respect to combination of weighting values (w_1, w_2): (a) for all 75 images and (b) for each group of images.

Table 1
Comparison of processing time: the previous dynamic programming method vs. the proposed method with different ROI sizes and rotation ranges of the directional Haar-like filter.

ROI size (width × height)	Previous DP mean ± std. (s)	Proposed method mean ± std. (s)		
		Rotation range of the filter		
		−15° to 15°	−30° to 30°	−45° to 45°
100 × 100	0.086 ± 0.001	1.776 ± 0.001	3.520 ± 0.003	5.253 ± 0.002
200 × 100	0.181 ± 0.005	3.546 ± 0.005	7.014 ± 0.006	10.466 ± 0.009
300 × 100	0.291 ± 0.012	5.335 ± 0.009	10.529 ± 0.02	15.708 ± 0.007

The processing time is summarized in Table 1, where the execution time was measured on different ROI sizes (100 × 100, 200 × 100, and 300 × 100) and rotation ranges of the proposed filter (−15° to 15°, −30° to 30°, and −45° to 45°). All our valuations were performed on an Intel Pentium Core™ 2 PC with a 2.53 GHz CPU and 2 GB of main memory. The processing time depends on the size of the ROI and the rotation range. The processing time of our method for rotation ranges −15° to 15°, −30° to 30°, and −45° to 45° was, respectively, 1.776, 3.520, and 5.253 s on average for the 100 × 100 ROI size, 3.546, 7.014, and 10.466 s for the 200 × 100 ROI size, and 5.335, 10.529, and 15.708 s for the 300 × 100 ROI size, while the time needed for the previous method was 0.086, 0.181, and 0.291 s for 100 × 100, 200 × 100, and 300 × 100 ROI sizes, respectively. As shown in Table 1, our method required longer times since the proposed filter is rotated around each pixel through angles within the range at 5° intervals. Although our method required more computation time than the previous method, it provided accurate results in boundary segmentation of sloping boundary, speckles, echo gap, and dropout found in ultrasound images, as shown in Fig. 15.

6. Conclusion

In this paper, we have proposed a semi-automatic method for detecting the boundary of the intima and adventitia of the carotid

artery in ultrasound images by a dynamic programming procedure based on a directional Haar-like filter, which replaces the intensity and intensity gradient previously used as the image features [8]. The directional Haar-like filter comprising the black and white region can correctly produce the minimum of the image feature by aligning the filter to the direction of the boundary. This method not only achieves accurate segmentation of sloping boundaries but also overcomes the problems caused by speckle noise and weak edges found in ultrasound images.

Experimental results show that our method accurately provides the segmented IMC. For accuracy evaluation, we compared our results with a manual method, which was performed by two experts. The average of errors between the boundaries extracted by the proposed method and the manual method ranged from 0.043 to 0.044 mm. The *p*-values of each IMT measurement, obtained by the paired *t*-test, show that there was no statistically significant difference between the manual and the proposed segmentation measurements. Therefore, our approach can be used successfully in the measurement of IMT, complementing the manual measurements and solving the problem of operator variability based on manual measurements while enhancing reproducibility. However, for more accurate clinical experiments, some interactive tools are still needed in order to correct some residual detection errors in extremely poor images.

Conflict of interest statement

None declared.

Acknowledgements

This work was partially supported by the National Research Foundation of Korea through the Acceleration Research Program and by the Ministry of Education and Human Resources Development (MOE), the Ministry of Commerce, Industry and Energy (MOCIE), and the Ministry of Labor (MOLAB) under the Fostering Project of the Lab of Excellency. We would like to thank the Medison Co. Ltd. for providing ultrasound image datasets for our experiments.

References

[1] H.N. Hodis, W.J. Mack, The role of carotid artery intima–media thickness in predicating clinical coronary events, Annals of Internal Medicine 128 (4) (1998) 262–269.
[2] M.L. Bots, D.E. Grobbee, A. Hofman, J.C.M. Witteman, Common carotid intima–media thickness and risk of acute myocardial infarction: the role of lumen diameter, Stroke 36 (4) (2005) 762–767.
[3] D.H. O'Leary, J.F. Polak, R.A. Kronmal, T.A. Manolio, G.L. Burke, S.K. Wolfson Jr., Carotid-artery intima and media thickness as a risk factor for myocardial infarction and stroke in older adults, The New England Journal of Medicine 340 (1999) 14–22.
[4] W.A. Riley, Carotid intima–media thickness: risk assessment and scanning protocol, European Heart Journal 23 (12) (2000) 916–918.
[5] R.H. Selzer, H.N. Hodis, H. Kwong-Fu, W.J. Mack, P.L. Lee, C.R. Liu, C.H. Liu, Evaluation of computerised edge tracking for quantifying intima–media thickness of the common carotid artery from B-mode ultrasound images, Atherosclerosis 111 (1994) 1–11.
[6] T. Gustavsson, Q. Liang, I. Wendelhag, J. Wilkstrand, A dynamic programming procedure for automated ultrasonic measurement of the carotid artery, IEEE Computers in Cardiology 21 (1994) 297–300.
[7] I. Wendelhag, Q. Liang, T. Gustavson, J. Wilkstrand, A new automated computerized analyzing system simplifies readings and reduces the variability in ultrasound measurement of intima–media thickness, Stroke 28 (11) (1997) 2195–2200.
[8] Q. Liang, I. Wendelhag, J. Wilkstrand, T. Gustavsson, A multiscale dynamic programming procedure for boundary detection in ultrasonic artery images, IEEE Transactions on Medical Imaging 19 (2) (2000) 127–142.
[9] D.C. Cheng, A. Schmidt-Trucksaess, K.S. Cheng, H. Burkhardt, Using snakes to detect the intimal and adventitial layers of the common carotid artery wall in sonographic images, Computer Methods and Programs in Biomedicine 67 (1) (2002) 27–37.
[10] L.D. Cohen, On active contour models and balloons, Computer Vision, Graphics, and Image Processing: Image Understanding 53 (2) (1991) 211–218.
[11] D.C. Cheng, X. Jiang, Using dual dynamic programming for artery's inner wall detection in sonographic images, in: Proceedings of the First International Workshop on Computer Vision for Intravascular and Intracardiac Imaging, 2006, pp. 138–145.
[12] C.P. Loizou, C.S. Pattichis, M. Pantziaris, T. Tyllis, A. Nicolaides, Snakes based segmentation of the common carotid artery intima media, Medical & Biological Engineering & Computing 45 (1) (2007) 35–49.
[13] A.A. Amini, T.E. Weymouth, R.C. Jain, Using dynamic programming for solving variational problems in vision, IEEE Transactions on Pattern Analysis and Machine Intelligence 12 (9) (1990) 855–867.
[14] P. Viola, M. Jones, Rapid object detection using a boosted cascade of simple features, in: Proceedings of the IEEE International Conference on Computer Vision and Pattern Recognition, 2001, pp. 511–518.
[15] W.H. Press, S.A. Teukolsky, W.T. Vetterling, B.P. Flannery, Numerical Recipes in C++: The Art of Scientific Computing, second edition, Cambridge University Press, New York, 2002.

Yu-Bu Lee received her B.S. degree (1990), M.S. degree (1992), and Ph.D. degree (2008) in Computer Science and Engineering at Ewha Womans University, Seoul, Korea. From 2008 to 2009, she was at the Sungkyunkwan University as a Post Doctor. Since 2009, she is a research professor in the Intelligent Systems Research Center at the Sungkyunkwan University, Suwon, Korea. Her current research interests include medical image processing and analysis, object recognition, and Human–Robot Interaction.

Yoo-Joo Choi received her B.S. degree (1989), M.S. degree (1991), and Ph.D. degree (2004) in Computer Science and Engineering at Ewha Womans University, Seoul, Korea. She is currently assistant professor of Seoul University of Venture and Information, Seoul, Korea. She was an assistant researcher at R&D Department of KCI Co. and POSDATA Co. of Korea between 1991 and 1999. Her current research interests include medical image processing, physically based modeling, visual simulation, virtual reality, and ubiquitous applications.

Myoung-Hee Kim received her Ph.D. degree (1986) from Universitaet Goettingen, Germany. She has been a professor in the Department of Computer Science and Engineering at Ewha Womans University, Korea, since 1987. Her current research interests include medical image segmentation, registration, visualization, simulation, and virtual reality.